UNIVERSITEIT·STELLENBOSCH·UNIVERSITY
jou kennisvennoot • your knowledge partner

Force and vibration analysis of magnetic gears
(repository copy)

Article:

Agenbach, C.J., Els, D.N.J., Wang, R-J., Gerber, S., (2018) Force and vibration analysis of magnetic gears, *XXIII International Conference on Electrical Machines*, (ICEM), pp. 752--758, 3-6 September 2018, Alexandroupoli, Greece

http://dx.doi.org/10.1109/ICELMACH.2018.8506690

Force and Vibration Analysis of Magnetic Gears

C. J. Agenbach, D. N. J. Els, R.-J. Wang and S. Gerber

Abstract—In this paper the analysis of unbalanced magnetic forces in magnetic gears are presented, based on which guidelines for identifying suitable pole-pairs and pole-pieces combinations for magnetic gear design with minimum unbalanced force are proposed. Furthermore, the vibration analysis is conducted on two prototype magnetic gears to evaluate the impact of unbalanced magnetic forces on their operational characteristics. It clearly shows that magnetic gear designs without unbalanced magnetic forces have less vibration and improved stability.

Index Terms—Flux modulation, force excitation frequency, gears, magnetic devices, magnetic flux, magnetic forces, vibrations, vibration measurement

I. INTRODUCTION

MECHANICAL gears have been widely used in a broad spectrum of industries. In recent years, an attractive new gear technology has come to the attention of researchers and engineers, namely the magnetic gear (MG). The renewed interest on MGs can be attributed to the increased availability of high energy permanent magnetic (PM) material, and more importantly the novel magnetic gear topologies [1]. The main advantages of MGs are: (i) the ability to operate with little or no lubrication, (ii) the built-in overload protection allowing the components of the MG to merely slip when overloaded, and (iii) the contact-less power transfer eliminating the frictional loss due to meshing teeth in conventional gears. Some comparative studies in literature [2], [3] show that magnetic gears can be a potential alternative to certain mechanical gear types.

A. Principles of Operation

The general layout of an MG can be seen in Fig. 1, which consists of an inner PM carrier, ferromagnetic pole pieces and an outer PM carrier. The ferromagnetic pole pieces (called a flux modulator) are the key to the magnetic gearing effects as they modulate the magnetic field thereby producing the field space harmonics in each air-gap corresponding to the adjacent PM pole-pairs. The number of ferromagnetic pole-pieces, q_m, and the number of PM pole-pairs on the inner and outer PM carriers, p_i and p_o respectively must satisfy

the following relationship to work with these asynchronous magnetic harmonics [4].

$$p_o = q_m - p_i \tag{1}$$

Any two of the three concentric components can be used as the input and output mechanical ports. Typical arrangements are to keep either the outer PM carrier or the flux modulator stationary. The resultant gear ratios are $G_r = 1 + p_o/p_i$ and $G_r = -p_o/p_i$, respectively. The negative sign in the latter implies that the outer and the inner PM carriers rotate in an opposite direction.

B. Unbalanced Magnetic Forces

Fractional gear ratios are usually preferred for MGs in order to realize smooth torque transmission [5]. However, for MGs with fractional gear ratios, there is often no magnetic symmetry, which can lead to radially unbalanced magnetic forces (UMF). As illustrated in Fig. 1, considering the magnetic forces between the three concentric components of an MG, a periodicity of at least two between the PM poles and the modulator pole pieces is required to avoid unbalanced radial forces [6], i.e.

$$f_{im} = \gcd\left(2p_i,\, q_m\right) \geq 2\,;\; f_{om} = \gcd\left(2p_o,\, q_m\right) \geq 2 \tag{2}$$

Although extensive research has been carried out on the various design aspects of MGs, there is relatively little published work on the UMFs and associated loss and vibration issues of MGs. The aim of this study is to analyze the forces and vibrations in MGs.
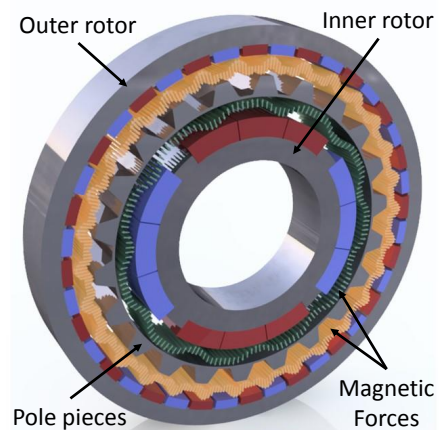

Fig. 1. The general layout of an MG (with exaggerated air-gaps) showing the magnetic forces.

II. FORCE ANALYSIS

A. Force Excitation Frequency

In an MG vibrations are generated by electromagnetic forces acting on a corresponding rotating component [7]. Thus, for a rotating modulator the major force excitation frequency is given by [8]:

$$f_{\text{excited, m}} = k\, q_m f_{r,\, m}\ (k = 1, 2, 3, ...) \tag{3}$$

Similarly, the main force excitation frequency for the inner PM carrier is:

$$f_{\text{excited, i}} = k\, p_i f_{r,\, i}\ (k = 1, 2, 3, ...) \tag{4}$$

where $f_{r,\, m}$ and $f_{r,\, i}$ are the rotational frequencies of the modulator and inner PM carrier, respectively.

B. Maxwell Stress Tensor Method

The Maxwell stress tensor is often used to calculate electric and magnetic forces on objects. For magnetostatic forces, the total force on an object may be expressed in terms of a volume integral of the force density as follows:

$$\vec{F} = \int_V \vec{f} dV \tag{5}$$

where the force density $\vec{f}$ is defined in [9] as

$$\vec{f} = \frac{1}{\mu} \nabla \cdot \mathbb{T} \tag{6}$$

The Maxwell stress tensor $\mathbb{T}$ is defined as

$$\mathbb{T} = T_{xx}\hat{\mathbf{x}}\hat{\mathbf{x}} + T_{xy}\hat{\mathbf{x}}\hat{\mathbf{y}} + T_{xz}\hat{\mathbf{x}}\hat{\mathbf{z}} + T_{yx}\hat{\mathbf{y}}\hat{\mathbf{x}} + T_{yy}\hat{\mathbf{y}}\hat{\mathbf{y}} + T_{yz}\hat{\mathbf{y}}\hat{\mathbf{z}}$$
$$+ T_{zx}\hat{\mathbf{z}}\hat{\mathbf{x}} + T_{zy}\hat{\mathbf{z}}\hat{\mathbf{y}} + T_{zz}\hat{\mathbf{z}}\hat{\mathbf{z}} \tag{7}$$

where $\hat{\mathbf{x}}$, $\hat{\mathbf{y}}$, and $\hat{\mathbf{z}}$ are the Cartesian unit vectors. Then it follows from (6) that

$$\vec{f} = \frac{1}{\mu}\left\{ \left(\frac{\partial T_{xx}}{\partial x} + \frac{\partial T_{xy}}{\partial y} + \frac{\partial T_{xz}}{\partial z}\right)\hat{\mathbf{x}} \right.$$
$$+ \left(\frac{\partial T_{yx}}{\partial x} + \frac{\partial T_{yy}}{\partial y} + \frac{\partial T_{yz}}{\partial z}\right)\hat{\mathbf{y}}$$
$$\left. + \left(\frac{\partial T_{zx}}{\partial x} + \frac{\partial T_{zy}}{\partial y} + \frac{\partial T_{zz}}{\partial z}\right)\hat{\mathbf{z}} \right\} \tag{8}$$

Furthermore, from [9] if a linear media is considered with a constitutive relation $\vec{B} = \mu\vec{H}$, the components of $\mathbb{T}$ are given as

$$[\mathbb{T}] = \begin{bmatrix} B_x^2 - \frac{1}{2}|B|^2 & B_x B_y & B_x B_z \\ B_y B_x & B_y^2 - \frac{1}{2}|B|^2 & B_y B_z \\ B_z B_x & B_z B_y & B_z^2 - \frac{1}{2}|B|^2 \end{bmatrix} \tag{9}$$

By substituting (6) into (5), we have

$$\vec{F} = \frac{1}{\mu} \int_V \nabla \cdot \mathbb{T} dV. \tag{10}$$

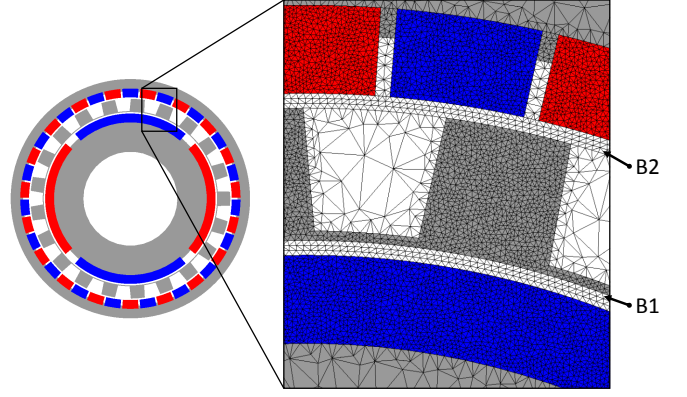From the divergence theorem, (10) can be written as a surface integral as follows:

Fig. 2. Integration paths in the FE model of the MG.

$$\vec{F} = \frac{1}{\mu} \oint_S \mathbb{T} \cdot \hat{\mathbf{n}} dS \tag{11}$$

where μ is the permeability of the medium through which the integration takes place, $\hat{\mathbf{n}}$ is the outward unit normal to the bounding surface, and the integration is performed over a surface S immediately surrounding the body. In principle, S should be the surface of the body itself. It is common in FE analysis to express these forces in cylindrical coordinates [7], [10], as

$$F_r = \frac{L}{2\mu_0} \oint_l (B_r^2 - B_t^2) dl \tag{12}$$

$$F_t = \frac{L}{\mu_0} \oint_l B_r B_t dl \tag{13}$$

where L is the stack length of the MG, B_r and B_t are the radial and tangential magnetic flux densities, respectively, and μ_0 is the magnetic permeability of the air-gap.

The calculation of the magnetic forces requires the knowledge of the Maxwell stresses along the circumference of each component. These stresses can be obtained from a FEM simulation model. To compute the forces, the stresses need to be integrated over a closed surface, which reduces to a closed path in a 2D Cartesian problem. Since the modulator experiences forces from both inner and outer PMs, the resultant force acting on the modulator is of particular interest for this study. As a result, the integration paths B1 and B2 (shown in Fig. 2) will be analyzed in detail. Fig. 3a and 3b show the space distribution of radial and tangential components of the stress along B1, respectively. Similarly, Fig. 4 shows the radial and tangential stress components along B2.

C. Force Integration

The resultant force in each air-gap contour was calculated by applying the Maxwell stress tensor method as discussed in section II-B, with a Python script and 4×10^4 sample points. To calculate the resultant forces, the stress components obtained in cylindrical coordinates can be transformed to Cartesian coordinates using (14).
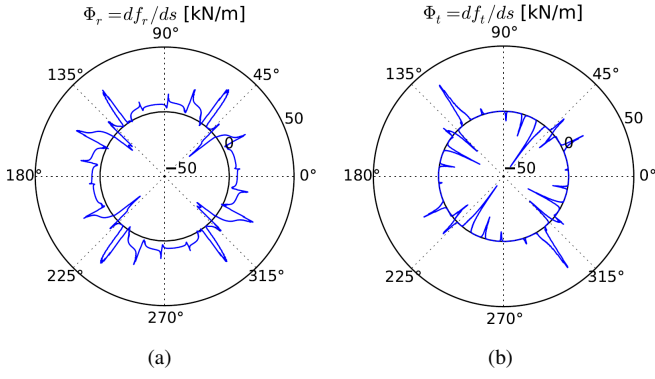
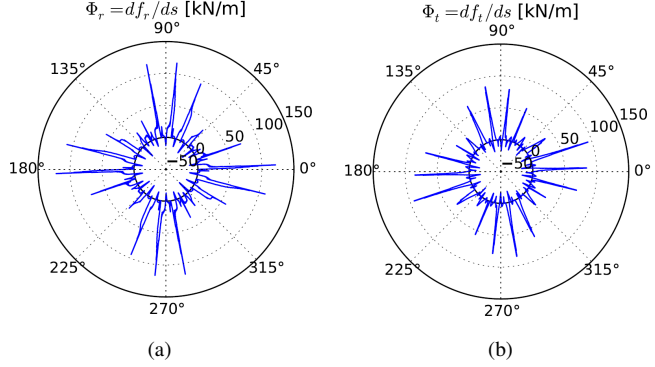Fig. 3. Force densities along B1: (a) Radial, (b) Tangential.

Fig. 4. Force densities along B2: (a) Radial, (b) Tangential.

$$\begin{bmatrix} \phi_x \\ \phi_y \end{bmatrix} = \begin{bmatrix} +\cos\theta & -\sin\theta \\ +\sin\theta & +\cos\theta \end{bmatrix} \begin{bmatrix} \phi_t \\ \phi_r \end{bmatrix} \qquad (14)$$

where ϕ_r and ϕ_t are the radial and tangential stress components, respectively while ϕ_x and ϕ_y are the corresponding xy stress components.

Then, by applying a transformation matrix the forces in the x and y directions can be obtained. This was done for B1 and B2 and the sum of the resultant forces were determined by adding the x and y forces, as given by (15) and (16), respectively. Furthermore, the magnitude and angle of the resultant force due to both air gaps were determined by applying (17) and (18), respectively.

$$F_{Tx} = F_{xB1} + F_{xB2} \qquad (15)$$

$$F_{Ty} = F_{yB1} + F_{yB2} \qquad (16)$$

$$F_R = \sqrt{F_{Tx}^2 + F_{Ty}^2} \qquad (17)$$

$$\theta = \arctan 2(F_{Ty}, F_{Tx}). \qquad (18)$$

D. Unbalanced Magnetic Force Analysis

Using the method described in the previous section, the unbalanced magnetic forces of MG designs with different gear ratios can be evaluated. Considering the MG design options for a gear ratio between 10:1 to 15:1, the calculated UMFs for different combinations of (p_i, p_o and q_m) are
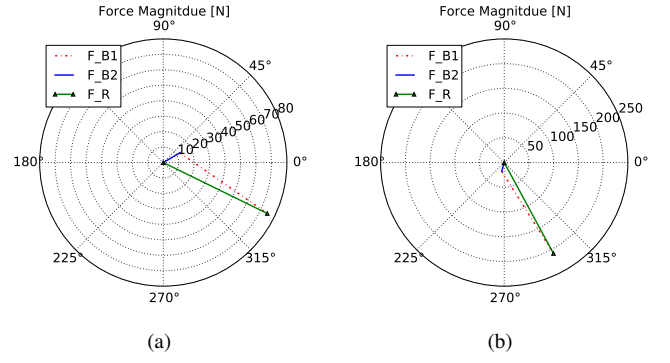

Fig. 5. The radial forces and their directions in the inner air-gap, outer air-gap and the resultant radial force on the modulator for: (a) the design with ($p_i = 2$, $p_o = 23$, $q_m = 25$), (b) the design with ($p_i = 2$, $p_o = 25$, $q_m = 27$).
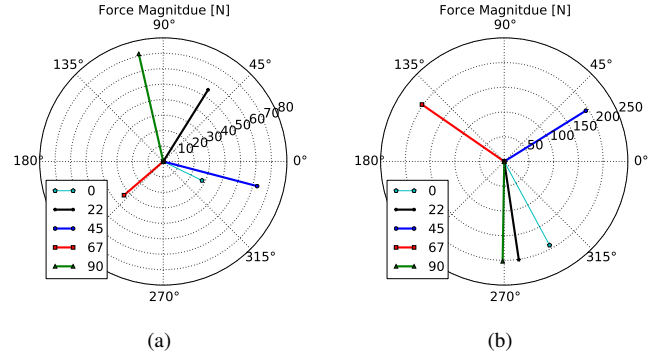

Fig. 6. The resultant radial force vectors at a number of inner rotor positions for: (a) the design with ($p_i = 2$, $p_o = 23$, $q_m = 25$), (b) the design with ($p_i = 2$, $p_o = 25$, $q_m = 27$).

summarized in Table I. Figs. 5a and 5b show the radial forces and their directions in the inner air-gap, outer air-gap and the resultant radial force (on the modulator) for two design cases. The resultant force vectors (magnitude and angle) at a number of inner rotor positions for each design are plotted in Figs. 6a and 6b, respectively. By comparing these two figures, it can be seen that the the magnitude of the resultant forces are also related to gear ratios.

Based on the MG designs presented in Table I a few interesting observations can be made:

- Designs with $f_{im} = f_{om} = 2$ have negligible UMFs while the designs with $f_{im} = f_{om} = 1$ are prone to large UMFs;
- Since f_{im} or f_{om} is equivalent to the cogging factor [6], $f_{im} = f_{om} = 2$ should be a good trade-off between UMFs and torque quality;
- MG designs free from UMFs can also be realized for fractional gear ratios. However, these designs are usually associated with higher pole-pairs counts, which implies higher electrical frequency and electromagnetic loss for the same mechanical speed.

From this analysis the importance of judicious selection of pole-pairs/pole-pieces combinations is clearly shown.

TABLE I
MG DESIGN OPTIONS FOR GEAR RATIOS BETWEEN 10:1 AND 15:1

p_i	p_o	q_m	Gr	UMF [N]	f_{im}	f_{om}
...	...	...	...	...	...	...
1	9	10	10	7	2	2
1	11	12	12	16	2	2
1	13	14	14	9	2	2
2	20	22	11	4	2	2
2	24	26	13	10	2	2
2	28	30	15	12	2	2
3	31	34	11.33	10	2	2
3	35	38	12.66	34	2	2
3	37	40	13.33	2	2	2
3	41	44	14.66	8	2	2
4	42	46	11.5	7	2	2
4	46	50	12.5	8	2	2
4	50	54	13.5	8	2	2
4	54	58	14.5	8	2	2
...	...	...	...	...	...	...
1	10	11	11	185	1	1
1	12	13	13	335	1	1
1	14	15	15	385	1	1
2	19	21	10.5	100	1	1
2	21	23	11.5	77	1	1
2	23	25	12.5	200	1	1
2	25	27	13.5	80	1	1
...	...	...	...	...	...	...

TABLE II
DESIGN PARAMETERS OF MG PROTOTYPES

Parameter	Prototype I	Prototype II
HS number of pole pairs	4	2
LS number of steel segments	15	22
PM carrier number of pole pairs	11	20
Gear outer radius [mm]	81.5	106
PM carrier yoke thickness [mm]	5.5	9
PM carrier magnet thickness [mm]	6	5
Modulator (LS) thickness [mm]	9	10
HS magnet thickness [mm]	6	10
HS yoke thickness [mm]	20	24
Modulator inner width [% pitch]	0.57	0.73
Modulator outer width [% pitch]	0.46	0.3
Modulator bridge thickness [mm]	0.65	0.35
Outer air-gap width [mm]	1.0	1.0
Inner air-gap width [mm]	1.0	1.0
PM carrier magnets volume [% area]	0.90	0.878
HS magnets volume [ratio of area]	0.90	0.865
Stack length [mm]	100	60
$(f_{im} ; f_{om})$	(1 ; 1)	(2 ; 2)
UMF [N]	160	4
Gear ratio	3.75:1	11:1
Peak torque [Nm]	254	254
Efficiency (rated)	94%	95%
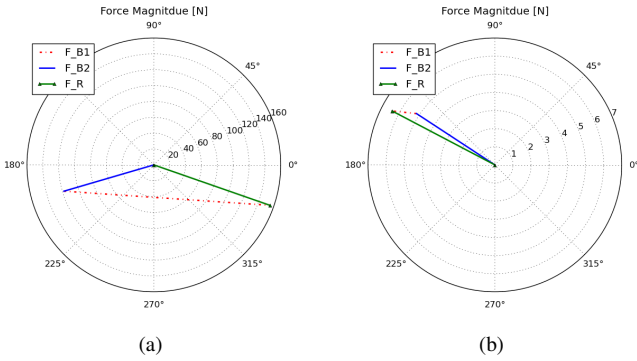
Fig. 7. The resultant radial forces on the modulator for: (a) prototype I, (b) prototype II.

Fig. 8. Exploded view of prototype I.

III. EXPERIMENTAL INVESTIGATION

To experimentally evaluate the UMFs and their impact on the MGs, two MG prototypes have been developed in the laboratory. Their respective design parameters are given in Table II. Figs. 7a and 7b show the resultant radial forces (on the modulator) for these two design cases. Prototype I [12] has a fractional gear ratio and an UMF in the region of 160 N while prototype II has an integer gear ratio and is free from UMF.

A. MG Prototype with UMFs

The basic experimental set-up for the first MG prototype is shown in Fig. 9, in which a variable-speed drive (VSD) as the prime mover and a second geared VSD induction motor drive running in regenerative mode as the load. The MG under test is connected between the two torque sensors. During the test, it was observed that t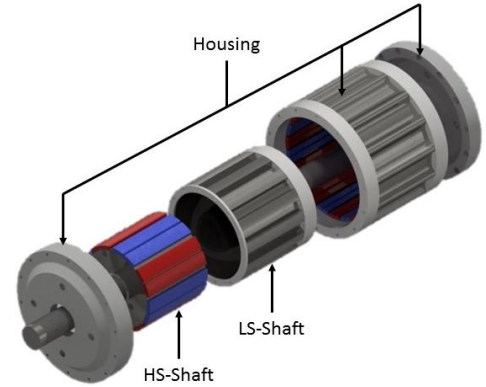here existed an eccentricity in the rotation of the low-speed rotor (modulator), which may be attributed to the large UMF.

A vibration analysis for prototype I was done at 600 rpm input speed and rated power of 2.2 kW. The accelerometers were mounted as shown in Fig. 9. A frequency sweep measurement from 5 Hz to 5 kHz was done to determine the excited frequency range, and it was observed that the most dominant frequencies were below 100 Hz. Thus, the frequency range was set to 100 Hz, and a sampling frequency of 200 Hz to avoid aliasing from occurring. A spectrogram of the MG is displayed in Fig. 10, which shows the integrity and quality of the measurement is constant over the entire reading. Fig. 11 shows a power spectral density (PSD) for the same signal.

Since the rotation frequency of LS rotor is 2.67 Hz at 160 rpm, the electromagnetic force frequencies are multiples of 40 Hz based on (3) [11]. The peaks from Fig. 11 can be identified from Table III, where the most dominant frequency
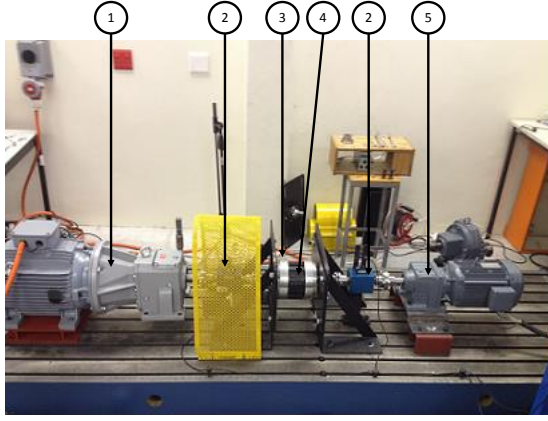
Fig. 9. Testing layout of prototype I, where 1- Geared induction motor, 2- Lorenz torque sensor, 3- Piezoelectric accelerometer, 4- Magnetic gear, 5- geared induction motor.
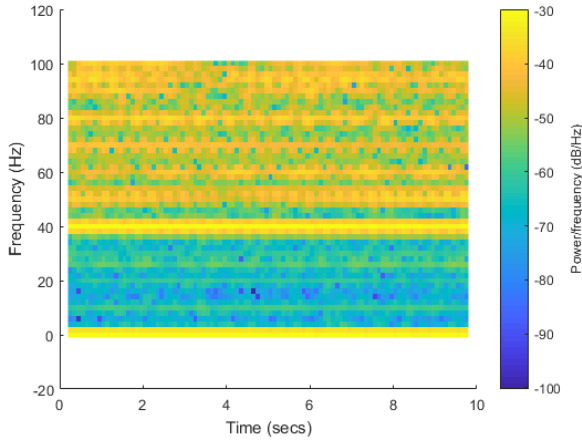

Fig. 11. PSD of prototype I at rated conditions.
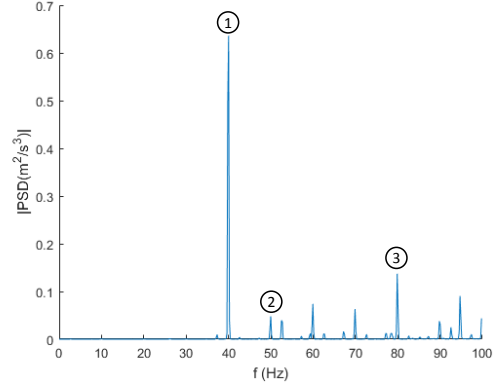

Fig. 10. Spectrogram of prototype I at rated conditions.
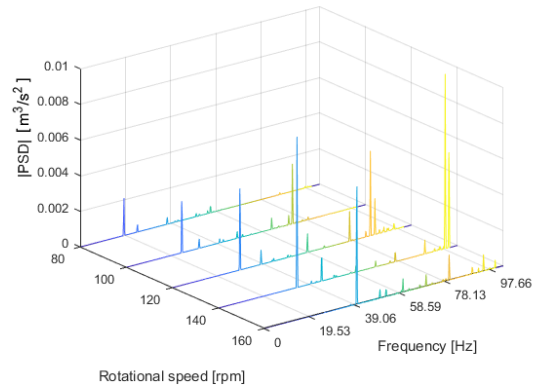
Fig. 12. PSD plots of prototype I at rated torque with varying speed.

is the electromagnetic force frequency responsible for radial deformation at $40\,\text{Hz}$, and amplitude of $0.7\,\text{m}^2/\text{s}^3$, while the rotor operating frequency cannot be seen.

Fig. 12 shows a series of the PSD plots at a constant torque as a function of frequency for different operating speeds, in which frequency is given on the x-axis, speed is given on the y-axis, and the PSD amplitude is shown on the z-axis. As the speed was increased the amplitude also increased and the most dominant frequency for all the measurements was found to be the MG pole frequency. It increased linearly with the speed from a frequency of $19.54\,\text{Hz}$ at $80\,\text{rpm}$ to a frequency of $39.06\,\text{Hz}$ at $160\,\text{rpm}$. It can also be seen that at

TABLE III
FREQUENCIES TO TAKE NOTE OF AT RATED CONDITIONS.

Label	Description	Value	Unit
-	Rotor operating frequency	10	Hz
1	LS radial force frequency	40	Hz
2	Motor frequency	50	Hz
3	2nd Harmonic of LS radial force frequency	80	Hz

the speeds $120\,\text{rpm}$ and $140\,\text{rpm}$ the system goes through a resonance at a frequency $85.80\,\text{Hz}$ and $97.66\,\text{Hz}$, respectively.

Fig. 13 shows a series of the PSD plots at constant speeds as a function of frequency for different torque values. It can be clearly seen that the amplitude of the vibration relates more to the operating speed and generally does not vary much with the load torque. Also, for a speed of $140\,\text{rpm}$, the system experienced higher frequencies at approximately $97\,\text{Hz}$. Therefore, this can be considered to be the natural frequency of the system.

B. MG Prototype without UMFs

Fig. 14 shows the exploded view of the prototype II design layout. A schematic of the test set-up configuration is given in Fig. 15. Prototype II was loaded with a custom designed fan (as a possible application for the MG).

A vibration analysis for prototype II was performed at $1500\,\text{rpm}$ output speed and rated power of $2.2\,\text{kW}$. The PSD at rated speed is given in Fig. 17, and gives the amplitude of the frequencies in m^2/s^3. The labels in Fig. 17 correspond to the measured values given in Table IV, while the calculated values were obtained as discussed previously. A spectrogram for rated output speed is given in Fig. 16 and clearly shows the excited frequencies presented in Table IV.
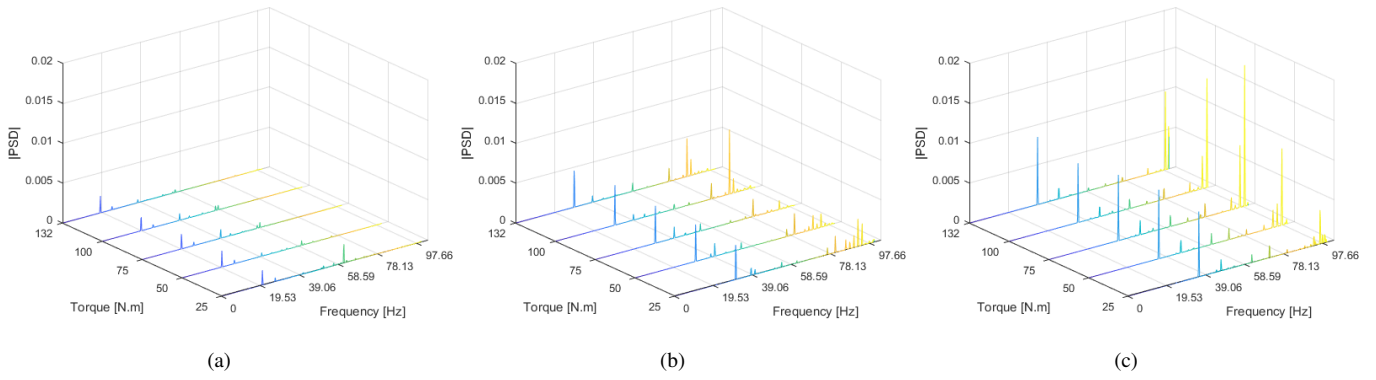
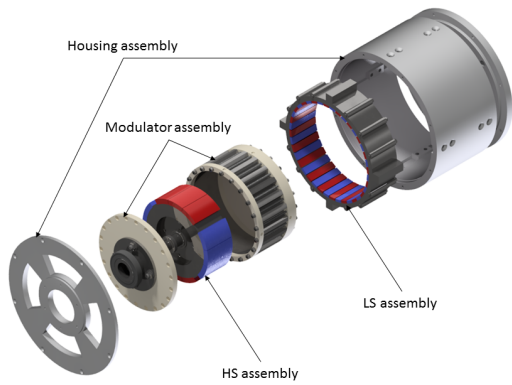Fig. 13. PSD plots of prototype I at constant speeds with varying torque: (a) 80 RPM (b) 120 RPM (c) 140 RPM.

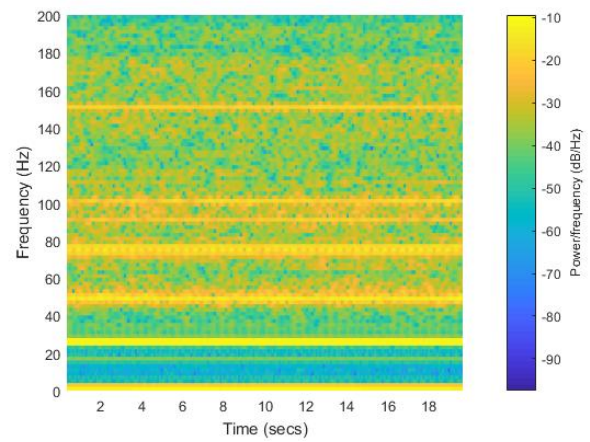Fig. 14. Exploded view of prototype II showing the assemblies.

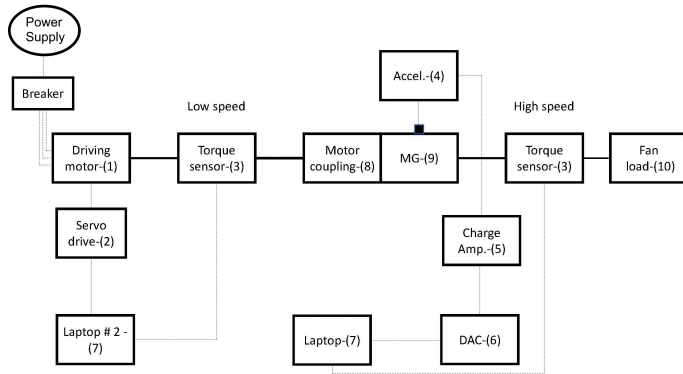Fig. 16. Spectogram of prototype II at rated conditions.

Fig. 15. Schematic of the test set-up for prototype II.

Thus, measured values compare well to the calculated values, where the dominant frequency ① relates to the operating speed of the output shaft, while ② is the excited frequency of the MG, and ③ is the HS bearing frequency. Furthermore, peak ④ is the frequency of the drive and peak ⑤ is the vane passing frequency of the fan. The excited frequency of the MG ② relating to the transmission forces was three times lower than the speed frequency ①. This implies that the vibrations relating to the transfer forces were reduced for the prototype II.
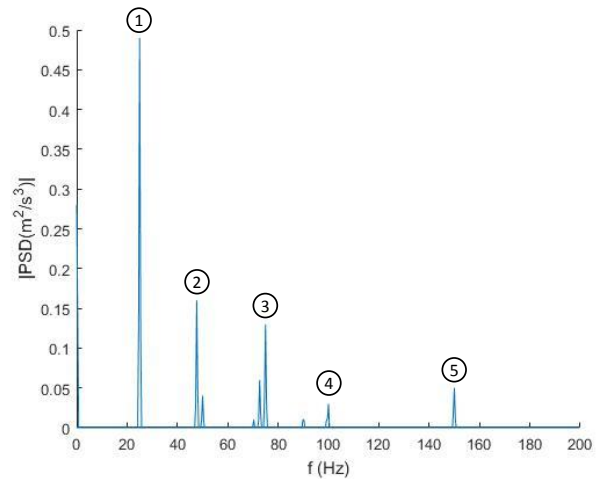

Fig. 17. PSD of prototype II at rated conditions.

TABLE IV
FREQUENCIES FOR PROTOTYPE II AT RATED CONDITIONS.

Label	Description	Calculated [Hz]	Measured [Hz]
1	Output speed	25	25
2	LS radial force frequency	50	48
3	HS bearing	82	75
4	Servo drive frequency	100	100
5	Fan vane frequency	150	150

IV. CONCLUSION

From these case studies it was showed that UMF can be problematic if not supported properly. Thus, it was decided to reduce UMF as far as possible in the design of prototype II with the aid of Table I. A vibrational analysis revealed the dominant frequency to be the operating speed of the output shaft for prototype II, while the amplitude of the excited frequency, relating to the transmission forces, of the MG was three times lower than the running speed. On the other hand, prototype I had a dominant frequency while the transmission forces and the operating speed could not be seen due to the dominance of the transmission forces. Thus, by comparison, the overall vibration RMS levels in prototype II were greatly reduced and the MG was stable during operation.

REFERENCES

[1] P.M. Tlali, R.-J. Wang, S. Gerber, "Magnetic gear technologies: a review," Proc. of International Conference on Electrical Machines, (ICEM), Berlin, Germany, pp. 544–550, 2014.

[2] E. Gouda, S. Mezani, H.B. Ahmed and S. Sire, "Comparative Study Between Mechanical and Magnetic Planetary Gears," IEEE Transactions on Magnetics, vol. 47, no. 2, pp. 439-450, 2011.

[3] M. Desvaux, B. Multon, L. Baghli and A. Rezzoug, "Behaviour comparison between mechanical epicyclic gears and magnetic gears," International Symposiu on Multibody Systems and Mechatronics, pp. 401–410. Springer, 2017.

[4] K. Atallah and D. Howe, "A novel high-performance magnetic gear", IEEE Transactions on Magnetics, vol. 37, no. 4, pp. 2844-2846, 2001.

[5] N.W. Frank and H.A. Toliyat, "Gearing ratios of a magnetic gear for marine applications", IEEE Electric Ship Technologies Symposium (ESTS), pp. 477-481, 2009.

[6] G. Jungmayr, J. Loeffler, B. Winter, F. Jeske and W. Amrhein, "Magnetic gear: radial force, cogging torque, skewing, and optimization," IEEE Transactions on Industry Applications, vol. 52, no. 5, pp. 3822-3830, 2016.

[7] J. Lee and J. Chang, "Analysis of the vibration characteristics of coaxial magnetic gear", IEEE Transactions on Magnetics, vol. 53, no. 6, pp. 1-4, 2017.

[8] S. Zuo, S. Mezani, F. Lin and X. Wu, "Noise analysis, calculation, and reduction of external rotor permanent-magnet synchronous motor," IEEE Transactions on Industrial Electronics, vol. 62, no. 10, pp. 6204-6212, 2015.

[9] E.P. Furlani *Permanent Magnet and Electromechanical Devices*. Published: New York: Academic Press. 2001.

[10] R. Islam and I. Husain, "Analytical model for predicting noise and vibration in permanent-magnet synchronous motors," IEEE Transactions on Industry Applications, vol. 46, no. 6, pp. 2346-2354, 2010.

[11] J. Lee and J. Chang, "Vibration and noise characteristics of coaxial magnetic gear according to low-speed rotor structure", Journal of Mechanical Science and Technology 31(6), pp. 2723-2728, 2017.

[12] A. Matthee, R-J. Wang, C.J. Agenbach, D.N.J. Els and M.J. Kamper, "Evaluation of a magnetic gear for air-cooled condenser applications," IET Electric Power Applications, vol. 12, no. 5, pp. 677-683, 2018.

V. BIOGRAPHIES

Charles Agenbach was born in Cape Town in South Africa, on July 23, 1992. He received his BEng degree in Mechanical Engineering from Stellenbosch University in 2015 and finished his MEng degree in Mechanical Engineering in December 2017 with the focus on the mechanical design and vibrational analysis of a magnetic gearbox.

Daniel Els graduated with a BEng degree in Mechanical Engineering from the University of Pretoria, South Africa in 1983. He received his PhD degree in Mechanical Engineering from Stellenbosch University in 2009 where he is currently a senior lecturer. His research interests include dynamics and design and optimization of mechanical systems.

Rong-Jie Wang received his PhD degree in Electrical Engineering from Stellenbosch University in 2003 where he is currently an Associate Professor. His research interests include special electrical machines, computer-aided design and optimization of electrical machines, thermal modeling of electrical machines and renewable energy systems. He was a co-author of the monograph Axial Flux Permanent Magnet Brushless Machines (Springer).

Stiaan Gerber was born in Bellville in South Africa on February 20, 1986. He received his PhD in Electrical Engineering at Stellenbosch University in 2015 where he is currently working as a post-doctoral researcher. His main interests in the engineering field are electrical machine design, numerical optimization, renewable energy power generation and finite element methods.